



## Indium Tin Oxide optical access for magnetic tunnel junctions in hybrid spintronic–photonic circuits

A Olivier, L Avilés-Félix, A Chavent, L Álvaro-Goómez, M Rubio-Roy, S Auffret, L Vila, B Dieny, Ricardo C. Sousa, I Prejbeanu

### ► To cite this version:

A Olivier, L Avilés-Félix, A Chavent, L Álvaro-Goómez, M Rubio-Roy, et al.. Indium Tin Oxide optical access for magnetic tunnel junctions in hybrid spintronic–photonic circuits. *Nanotechnology*, 2020, 31 (42), pp.425302. 10.1088/1361-6528/ab9c56 . hal-03111547

**HAL Id: hal-03111547**

**<https://hal.science/hal-03111547>**

Submitted on 2 Feb 2021

**HAL** is a multi-disciplinary open access archive for the deposit and dissemination of scientific research documents, whether they are published or not. The documents may come from teaching and research institutions in France or abroad, or from public or private research centers.

L'archive ouverte pluridisciplinaire **HAL**, est destinée au dépôt et à la diffusion de documents scientifiques de niveau recherche, publiés ou non, émanant des établissements d'enseignement et de recherche français ou étrangers, des laboratoires publics ou privés.

# Development of optical access for magnetic tunnel junctions in hybrid spintronic–photonic circuits

A. Olivier, L. Avilés-Félix, A. Chavent, L. Álvaro-Gómez,  
M. Rubio-Roy, S. Auffret, L. Vila, B. Dieny, R.C. Sousa,  
I.L. Prejbeanu

Univ. Grenoble Alpes, CEA, CNRS, Spintec, 38000 Grenoble, France

E-mail: aurelien.olivier@cea.fr

March 2020

**Abstract.** The all-optical magnetization reversal of magnetic layers, by picosecond optical pulses, is of particular interest as it shows the potential for energy-efficient and fast magnetic tunnel junction (MTJ) elements. This approach requires memory elements that are optically and electronically accessible, for optical writing and electronic read-out. In this paper, we propose the integration of indium tin oxide (ITO) as a transparent conducting electrode for magnetic tunnel junctions in integrated spintronic – photonic circuits. To provide light with sufficient energy to the MTJ free layer and allow electrical read-out of the MTJ state, we successfully integrated indium tin oxide as a top transparent electrode. The study shows that ITO film deposition by physical vapor deposition with conditions such as high source power and low  $O_2$  flow achieves smooth and conductive thin films. Increases in grain size was associated with low resistivity. Deposition of 150 nm ITO at 300 W,  $O_2$  flow of 1 sccm and  $8.10^{-3}$  mbar vacuum pressure results in  $4.8 \times 10^{-4} \Omega \cdot \text{cm}$  resistivity and up to 80% transmittance at 800 nm wavelength. The patterning of ITO using  $CH_4/H_2$  chemistry in a reactive ion etch process was investigated showing almost vertical sidewalls for diameters down to 50 nm. The ITO based process flow was compared to a standard magnetic tunnel junctions fabrication process flow based on Ta hard mask. Electrical measurements validate that the proposed process based on ITO results in properties equivalent to the standard process. We also show electrical results of magnetic tunnel junctions having all-optical switching top electrode fabricated with ITO for optical access. The developed ITO process flow shows very promising initial results and provides a way to fabricate these new devices to integrate all-optical switching magnetic tunnel junctions with electronic and photonic elements.

## 1. Introduction

Magnetic random access memories (MRAM) are based on magnetic tunnel junction (MTJ) devices, having two ferromagnetic electrodes, a storage and a reference layers, separated by a ultrathin tunnel barrier [1]. MRAM is best known for its non-volatility, low energy consumption, high endurance, and compatibility with advanced silicon (Si) complementary metal-oxide-semiconductor (CMOS) processing. Conventional spin transfer torque (STT) MRAM cells use current to reverse the magnetization of the storage electrode. Recent studies have demonstrated the possibility of all-optical switching (AOS) of the magnetization direction in ferrimagnet systems having two magnetic sublattices antiferromagnetically coupled [2, 3]. These material systems open the possibility of writing with short laser pulses in the pico- and femto-second range even in the absence of applied magnetic field. Practical implementation of this concept to MRAM cells requires first the integration of AOS electrodes in a magnetic tunnel junction and second providing an optical access to the storage electrode in patterned cells. For the latter, the choice of the transparent material depends on its compatibility to be used as a hard mask during the ion beam etch step of the magnetic tunnel junction pillar. Possible transparent conductive oxides (e.g.  $\text{SnO}_2$ ,  $\text{In}_2\text{O}_3$  and  $\text{ZnO}$ ) have been widely used for this purpose [4]. Indium tin oxide (ITO) ( $\text{In}_2\text{O}_3\text{-SnO}_2$ ) is also commonly used as transparent conductive material, because of its low electrical resistivity and a high transparency [5]. ITO is also easy to pattern by reactive ion etching using (RIE)  $\text{CH}_4/\text{H}_2$  gas mix [6, 7, 8] and is more robust compared to  $\text{ZnO}$ , which is sensitive to moisture [4, 9]. This work demonstrates a successful process flow for the deposition and patterning of ITO used as hardmask to fabricate sub-100 nm diameter magnetic tunnel junctions. The optical access process is compared to our standard metallic hard-mask based MTJ nanofabrication in terms of dispersion and absolute electrical performance, showing better or comparable values for the optical access process.

## 2. ITO process flow development

A MTJ device is a two terminal pillar device usually defined by ion beam etching (IBE) using a metal hard mask. Tantalum (Ta) is commonly used as hardmask due to its robustness during ion milling, possibility to define sub-10 nm [10] pillar sizes and relatively low resistivity [1]. The process flow sequence is summarized in Figure 1 showing the Ta and ITO flows side by side. The main difference resides in the hardmask material and their corresponding deposition and etch steps. These steps were optimized

independently on both Si or quartz substrates. The results of this optimization are presented and discussed in the following sections.

### 2.1. ITO deposition optimization

In order to investigate the morphology, electrical and optical properties of ITO, thin films were deposited by physical vapor deposition (PVD) using an  $\text{In}_2\text{O}_3(90\%)/\text{SnO}_2(10\%)$  target and substrate holder at room temperature (RT). Prior to the deposition, a cleaning treatment based on acetone and isopropyl-alcohol (IPA) in ultrasonic bath is performed on all the samples. Surface morphology was investigated by scanning electron microscopy (SEM), the sheet resistance and electrical resistivity were characterized by co-linear four-point probe technique (4Dimensions Probe Model 280), the transmittance and reflectance evaluated using a spectro-photometer (Agilent Technologies Cary 7000) in the 0.2-2  $\mu\text{m}$  wavelength range. The ITO surface was observed for varying deposition conditions of target source power, pressure and  $\text{O}_2$  flow in the PVD chamber. SEM images of the top surface and cross section of 150 nm thin films deposited on a Ta/Pt buffer are shown in Figure 2. Deposition conditions for Figure 2(a-c) images correspond to increasing source power levels (100, 200 and 300 W) at constant 1 sccm  $\text{O}_2$  gas flow and  $8.10^{-3}$  mbar pressure. We observe two distinct grain morphologies: small grain sizes at low power and larger grain sizes at 300 W deposition power. Square base pyramid crystalites form on the surface of the ITO film. For a deposition power of 300 W, removing the  $\text{O}_2$  flow or reducing the pressure to  $2.10^{-3}$  mbar changes the grain morphology from a mix of small and large grains to only small grains, as shown respectively in Figure 2(d-e). Without  $\text{O}_2$  flow large crystalites disappear and the surface becomes smoother. Low pressure conditions also result in small grains without formation of crystalites, however the surface is much rougher compared to standard or no  $\text{O}_2$  flow conditions.

We measured ITO film sheet resistance  $R_S$  and resistivity  $\rho$ , using the relationship:  $\rho = R_S \cdot t$ , where  $t$  is the film thickness assumed to be uniform. Results are shown in Figure 3 and are consistent with SEM observations. For a reference of 1 sccm  $\text{O}_2$  flow and a deposition pressure of  $8.10^{-3}$  mbar the resistivity increases with the reduction of the source power. The lowest sheet resistance of  $32 \Omega/\square$  is obtained for 300 W and it increases to  $72 \Omega/\square$  for 100 W corresponding to resistivities of  $4.8 \times 10^{-4}$  and  $1.08 \times 10^{-3} \Omega\cdot\text{cm}$  respectively. The lower resistivity obtained at high power can be explained by the larger grain size observed for 300 W deposition conditions. According to Kim et al. [11], larger grain sizes

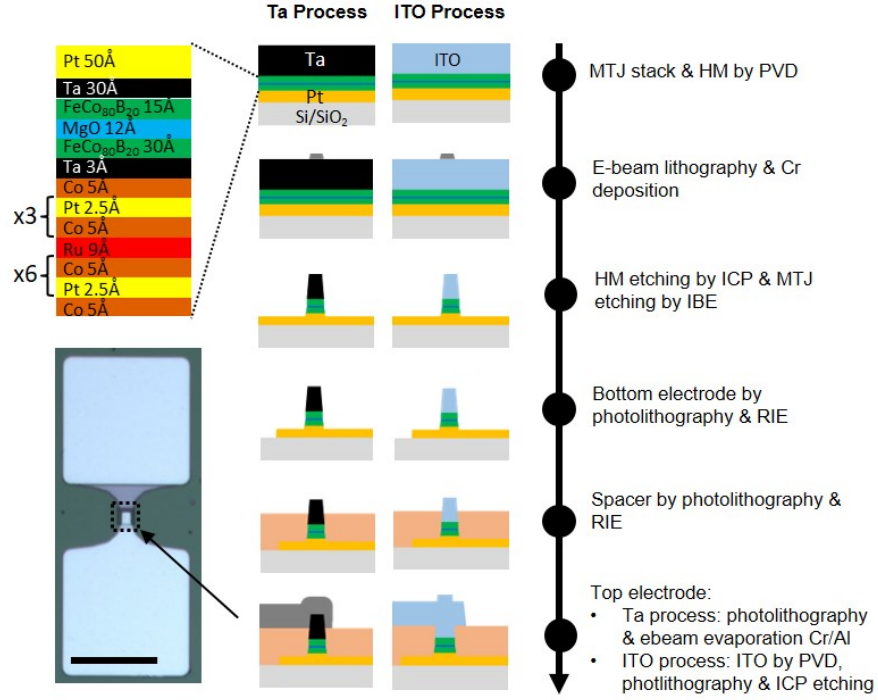


**Figure 1.** Process flows of Ta hard mask based MTJ with Cr/Al metallic electrode (Ta Process) and a proposed ITO based hard mask and top electrode (ITO Process). The magnetic stack is detailed on the top left. In bottom left, optical microscopy image of a MTJ (scale bar: 100  $\mu\text{m}$ ).

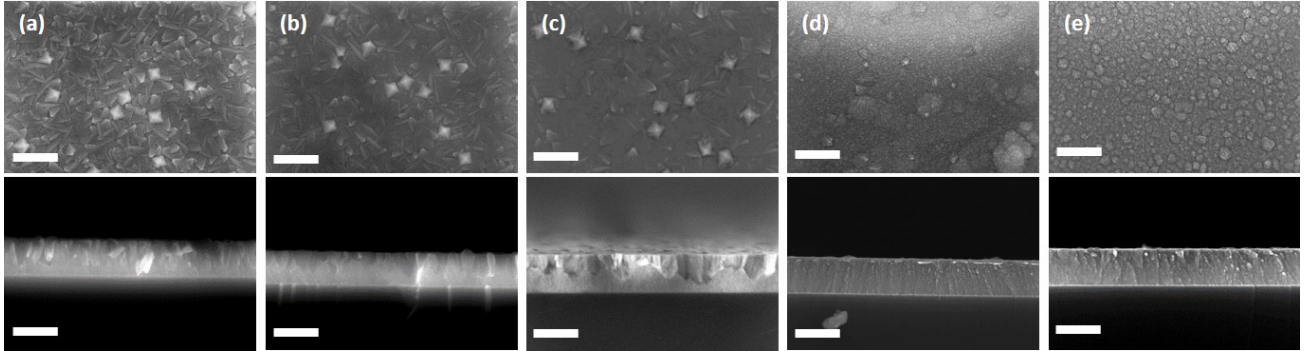


**Figure 2.** Top and cross-section view SEM images of the deposition of 150 nm of ITO by PVD on Si/SiO<sub>2</sub>/Ta(5 nm)/Pt(5 nm) substrates with different deposition conditions: (a) 100W/O<sub>2</sub>=1 sccm/p=8.10<sup>-3</sup>mbar, (b) 200W/O<sub>2</sub>=1 sccm/p=8.10<sup>-3</sup>mbar, (c) 300W/O<sub>2</sub>=1 sccm/p=8.10<sup>-3</sup>mbar, (d) 300W/O<sub>2</sub>=0sccm/p=8.10<sup>-3</sup>mbar and (e) 300W/O<sub>2</sub>=1 sccm/p=2.10<sup>-3</sup>mbar (scale bar: 100 nm).

correspond to lower sheet resistance and resistivity values, when the conductivity is limited by grain boundary scattering. This corresponds to our own observations of grain size dependence on deposition power as shown in Figure 2. The same effect was also observed for other TCO materials, as reported for example in ZnO [12]. Samples deposited at lower pressure (2.10<sup>-3</sup> mbar) or no oxygen flow, result in higher values of sheet resistance compared to the reference deposition conditions.

Low cristallinity with no O<sub>2</sub> flow was already associated to severe oxygen deficiencies in ITO, resulting in poor crystalline properties [13]. Our values of resistivity values are in same range of previous reports for the same Sn content (i.e. 10% wt.), thickness and substrate temperature [5, 14] but higher compared to the state of the art ( $7.2 \times 10^{-5} \Omega \cdot \text{cm}$ ) [15].

The influence of the Ta/Pt seed layer on the resistivity was evaluated by comparing the ITO resistivity for depositions on quartz substrates using

reference deposition conditions. Low pressure and no oxygen flow conditions were not repeated, since they resulted in higher ITO resistivity, which is undesirable for our application. The resistivity results and behavior as function of the deposition power are very similar to samples deposited on a Ta/Pt buffer, with both types of samples show resistivity differences less than 10%. The best results in terms of resistivity and surface morphology are again obtained for a source power of 300 W at a pressure of  $8.10^{-3}$  mbar and 1 sccm  $O_2$  flow. For quartz substrates the lowest resistivity obtained was  $5.25 \times 10^{-4} \Omega \cdot \text{cm}$ . These values of ITO resistivity are more than one order of magnitude higher compared to our standard Ta hard mask ( $\rho \sim 2.2 \times 10^{-5} \Omega \cdot \text{cm}$ ). However, for our typical hardmask dimensions it translates to about  $0.8 \Omega \cdot \mu\text{m}^2$  series contact resistance, smaller than the tunnel junction typical resistance area products of  $10\text{-}100 \Omega \cdot \mu\text{m}^2$ .

Optical properties of our ITO films were also investigated by measuring transmittance values. The transmittance data are shown on Figure 4 for different ITO thickness, deposition power and Pt capping layer thickness.

High absorption is measured below 500 nm wavelength due to the quartz substrate itself. A similar average transmittance of 80% is obtained for wavelengths between 500 and 1200 nm, independently of the deposition power. Differences induced by the deposition power are observed near infrared region above 1200 nm wavelength, the transmission decreasing for higher deposition power. At 1550 nm, a common laser wavelength, the transmittance decreases from 82% to 74%, for deposition powers of 100 and 300 W. This decrease can be explained by our previous observations on the surface morphology and

electrical resistivity. The cut-off wavelength  $\lambda_p$  can be considered as the point where the transmittance equals reflectance (not shown here). At large wavelengths, transmittance decreases faster for higher deposition powers. It can be extrapolated that higher deposition powers result in lower values of  $\lambda_p$ . This trend has been confirmed in previous studies [4, 5, 11]. The value of  $\lambda_p$  is inversely proportional on the carrier concentration  $N$  as follows:

$$\lambda_p = 1.24e/(\hbar\omega_p) \quad (1)$$

with,

$$\omega_p^2 = (4\pi Ne^2)/(\epsilon_0\epsilon_\infty m_e^*), \quad (2)$$

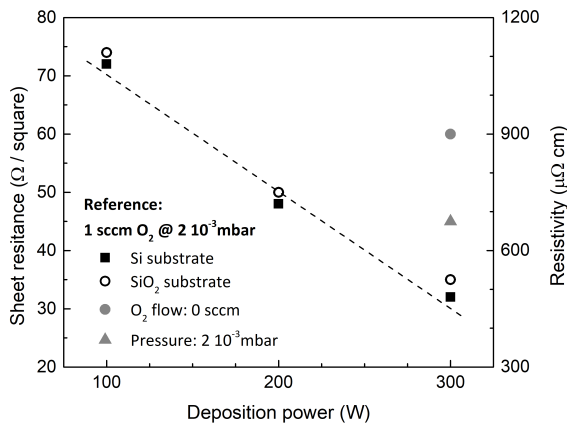
where  $e$  is the electron charge,  $\epsilon_0$  and  $\epsilon_\infty$ , respectively the dielectric constant of the medium and free space, and  $m_e^*$  the effective electron mass. Therefore, lower resistivity values associated with higher carrier concentration result in lower values of  $\lambda_p$ . This is again consistent with our observations, that high deposition power results in lower resistivity and also lower cut-off wavelength. The influence of ITO thickness is shown on Figure 4(b) for possible hardmask total thicknesses from 50-300 nm. For reference deposition conditions of 300 W /  $O_2=0$  sccm /  $p=8.10^{-3}$  mbar, at 1550 nm wavelength a transmittance of 84% is obtained for 50 nm and 71% for 150 nm, our standard hardmask thickness.

Finally, the influence of a possible Pt capping layer to prevent surface oxidation was investigated, with transmittance results shown in Figure 4(c). The impact of the Pt capping is very significant, the transmittance measured at 1550 nm decreasing from 71% for 150 nm ITO reference film, to 53% with a 2 nm Pt capping layer. The increased attenuation with the Pt capping is not an acceptable trade-off, since the improvement in electrical resistivity is marginal compared to the sample without Pt capping.

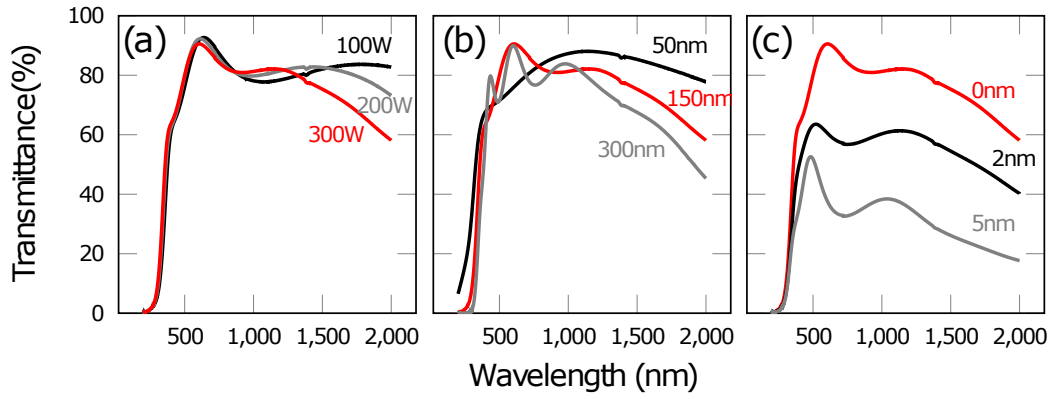
Based on these results, the reference process of 300 W /  $O_2=1$  sccm /  $8.10^{-3}$  mbar was defined as best trade-off to achieve low resistivity and high optical transmission. The total hardmask thickness was set at 150 nm without protection capping layer.

## 2.2. ITO etching

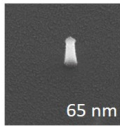
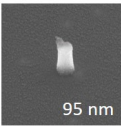
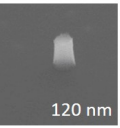
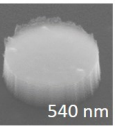
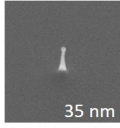
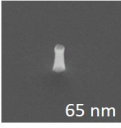
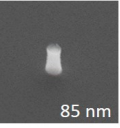
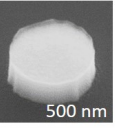
To define the ITO hardmask, the ITO film has to be etched to pillars having height/diameter aspect ratios up to 3. The samples for the ITO reactive ion etching study are prepared similarly with the reference deposition conditions mentioned in the previous section. The process flow illustrated in Figure 1, starts with an e-beam lithography step to define the pillar lateral size. A 20 nm Cr metal mask is defined in a lift-off process to be used as mask in



**Figure 3.** Sheet resistance and resistivity of ITO deposition at PVD different deposition conditions.



**Figure 4.** Transmittance spectra of ITO layer deposited on quartz substrates at the following PVD conditions, Ar = 39 sccm, O<sub>2</sub>=1 sccm, p=8.10<sup>-3</sup> mbar with (a) a thickness of 150 nm and different PVD power deposition; (b) different thicknesses of ITO at 300W and (c) of 150 nm ITO at 300 W with different Pt insertion thicknesses.

Nominal Diameter	50 nm	80 nm	100 nm	500 nm
ICP etch	 65 nm	 95 nm	 120 nm	 540 nm
IBE	 35 nm	 65 nm	 85 nm	 500 nm

**Figure 5.** Tilted view SEM images (angle at 45°) of the etching by ICP of the ITO pillars and their robustness through IBE process with multi-angle etching. Obtained average diameters after ICP and IBE are indicated (in white) in comparison to the nominal diameters relative to the design layout.

during the ITO etch. The Cr disks have nominal diameters from 20 up to 500 nm. Induced coupled plasma (ICP) has been applied successfully to etch ITO [6, 7, 8] in micron size feature patterns. For our deep sub-micron dimensions we used ICP plasma etching (Oxford Plasma Lab) based on a CH<sub>4</sub>/H<sub>2</sub> chemistry. The plasma conditions were: 50 sccm CH<sub>4</sub>, 20 sccm H<sub>2</sub>, 10 mTorr pressure, 1000 W ICP and 200 W RF power, at a controlled wafer temperature of 60°C. The etching progress is monitored by laser reflectometry for endpoint detection purposes. SEM images of patterned ITO pillars after the ICP etch step are shown in Figure 5. The etch is highly anisotropic with almost straight sidewalls (80°±3) and good yield is obtained starting at height/diameter ratios of ≈ 2.5. The endpoint selectivity was tested with Pt, but other materials such as SiO<sub>2</sub>, Si<sub>3</sub>N<sub>4</sub> can also be used as etch stop layer [16]. The etch rate was ≈ 75 nm/min, corresponding to about 120 s to etch 150 nm of ITO.

The process is followed by multi-angle ion beam

etching (IBE) with 3 sccm Ar flow and 200 W RF power. The IBE etch angle sequence used in the ITO process flow is the same as the one of our standard Ta hardmask flow. The magnetic tunnel junction multilayer is first etched with a predominantly vertical etch angle of 70° for about 2 min until the MgO tunnel barrier layer level is detected by secondary ion mass spectroscopy (SIMS). The etch angle is then changed to 45° to prevent re-deposition of metallic layers across the MgO tunnel barrier that result in a decrease of tunnel magnetoresistance (TMR) signal amplitude. Finally, once the magnetic layer stack has been completely etched, a grazing angle etch at 10° is performed for 45 s.

After IBE, the ITO pillar diameter was measured from SEM images shown in Figure 5, to reveal a lateral size reduction of 15-20 nm. This is the result of trimming happening during the IBE process and is common to both ITO and Ta process flows. It was also confirmed that after IBE the Cr mask used to pattern the ITO pillar was completely consumed during this step. Energy dispersive X-ray (EDX) measurements present no traces of Cr on top of the ITO. This is important since any metal layer will result in additional light loss, as was confirmed by our experiments, even for 2 nm Pt capping layers.

### 2.3. ITO top contact lead

The final necessary process flow modification for full optical access is to use an ITO top contact lead. This step was done by depositing ITO followed by photolithography and ITO reactive ion etching (RIE). ITO top lead thickness was 150 nm, deposited by PVD using reference deposition conditions. For the ITO etch step the same ITO hardmask RIE etch conditions were used. The etch endpoint is controlled by laser interferometry, relying on the etch selectivity of ITO



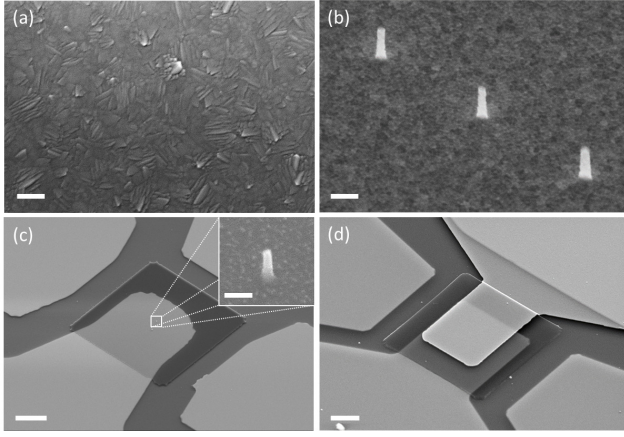


**Figure 6.** (a) Top view SEM image of ITO on magnetic stack (scale bar: 100 nm), (b) Tilted view SEM image of ITO pillars after IBE of the magnetic stack (scale bar: 100 nm) (c) Tilted view SEM image of MTJ device after thinning the Accuflo™ (scale bar: 4  $\mu\text{m}$ ) ITO pillar in inset (scale bar: 100 nm) and (d) Tilted view SEM image of the top electrode after by ICP (scale bar: 4  $\mu\text{m}$ ).

and the  $\text{SiO}_2$  substrate layer and an Accuflo™ spacer layer near the tunnel junction.

A summary of the main changes introduced in the ITO process flow are illustrated in Figure 6 by SEM images obtained at critical process steps. First the surface of the ITO film deposited on the magnetic stack is mostly uniform without significant topography that may be caused by crystalite growth (Figure 6(a)). The ITO pillar after RIE and IBE etch showing 50 nm diameter pillars is shown in Figure 6(b). A zoom of the tunnel junction area after patterning of the bottom lead is shown in Figure 6(c). On the same picture it is also possible to illustrate the Accuflo™ spacer layer providing for electrical isolation in the overlap region of the top and bottom leads. The complete device with the ITO top contact lead is shown in Figure 6(d).

### 3. Electrical evaluation of ITO process flow

The ITO process flow was compared against the Ta metal hardmask flow on conventional perpendicular anisotropy magnetic tunnel junctions. The tunnel junction stack was composed of a synthetic antiferromagnet (SAF) reference layer and a top Fe-CoB electrode having perpendicular surface anisotropy from the MgO barrier interface. The full magnetic stack was as follows: Pt(25)/ Co(0.5)/ [Pt(0.25)/ Co(0.5)]<sub>6</sub>/ Ru(0.9)/ [Pt(0.25)/ Co(0.5)]<sub>3</sub>/ Co(0.5)/ Ta(0.3)/ FeCo<sub>80</sub>B<sub>20</sub>(3)/ MgO(1.2)/ FeCo<sub>80</sub>B<sub>20</sub>(1.5)/ Ta(0.3)/ Pt(5), all thickness values in nm. We process two samples with identical stacks deposited on 50 mm wafers and annealed at 350°C for 2 min. Their expected tunnel magneto-resistance (TMR) and resis-

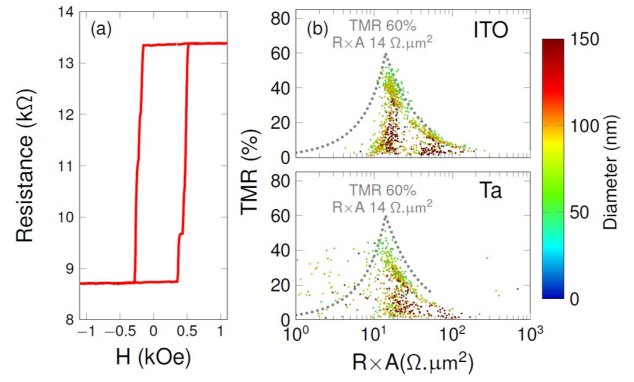


**Figure 7.** (a)  $R(H)$  hysteresis loop of a 80 nm nominal diameter MTJ device. (b) TMR plot with  $R_{\min}$  for different MTJ diameters comparison between ITO based devices process (ITO) and standard MTJ devices process (Ta). Dispersion in the TMR and  $R \times A$  as calculated from shunt and series resistance models (gray lines) are also shown.

tance area product ( $R \times A$ ) were measured by magneto-resistance current in-plane (MRCIP) technique to be 60% and 14  $\Omega \cdot \mu\text{m}^2$ . The samples are then covered either by a 150 nm Ta or ITO layer. The IBE process steps were identical for both wafers, a multi-angle IBE etch as follows: 70°/45°/10°. The TMR and  $R \times A$  values are shown in Figure 7 for both wafers. It is possible to achieve the maximum expected TMR for both process flows. The signature of two process problems can also be identified on both samples. For  $R \times A$  higher than the expected wafer value, the TMR signal is limited by a contact resistance associated with the hardmask top lead interface, measured in series with the actual tunnel junction resistance. For lower  $R \times A$  values, the TMR decrease on measured  $R \times A_{\text{meas}}$  follows a dependence that can be explained by current shunting across the tunnel barrier, due to some amount of metal re-deposition on the tunnel junction sidewalls. It is possible to model the expected TMR boundaries of both these process issues as follows:

$$TMR_{\text{series}} = TMR_0 \frac{RA_0}{RA_{\text{meas}}} \quad (3)$$

$$TMR_{\text{shunt}} = \frac{TMR_0 \times rs}{(1 + TMR_0) RA_0 + rs} \quad (4)$$

$$rs = \frac{RA_0 RA_{\text{meas}}}{RA_0 - RA_{\text{meas}}} \quad (5)$$

with  $TMR_0$  and  $R \times A_0$  being the potential wafer TMR and  $R \times A$  product. Data below these limit lines correspond to devices affected to some extent by both factors. An improved IBE etch and etch cleaning of the hardmask prior to the top electrode deposition eliminates these issues, as will be shown in the last section. A typical high squareness hysteresis loop is shown in Figure 7(a) for a 80 nm diameter

perpendicular anisotropy magnetic tunnel junctions and spin transfer torque (STT), having a TMR of 60%. A shift towards lower resistance values is observed for Ta compared to the ITO process. This can be due to a small variation of the tunnel barrier thickness or a smaller tunnel junction sizes in the ITO sample.

A closer analysis of both process flows was done based on the cumulative distribution functions (CDF) of both process flows, since it is then possible to quantify differences in device TMR yield. For all analyzed diameters from 50 up to 150 nm, the ITO process achieves TMR yields as good as or better compared to the Ta hardmask process. The results are shown for the different junction sizes in Figure 8, with smaller junction sizes having higher TMR yield for the ITO process flow. Typically a 10% higher TMR value can be observed at equivalent probability values. Our analysis does not allow to state that the ITO flow improves process yield, since the difference might be related to the observed  $R \times A$  shift. That might be related to smaller junction sizes with the Ta hardmask. However, it is clear that the ITO process achieves yields that are comparable to the reference process flow. Our result is to our knowledge the first time that ITO has been used as hard mask to define sub-100 nm magnetic tunnel junctions, achieving diameters as small as 50 nm.

### 3.1. ITO flow on all optical switching magnetic stack

The goal of developing an ITO based process flow was to fabricate magnetic tunnel junctions allow for an optical access to the top electrode. The

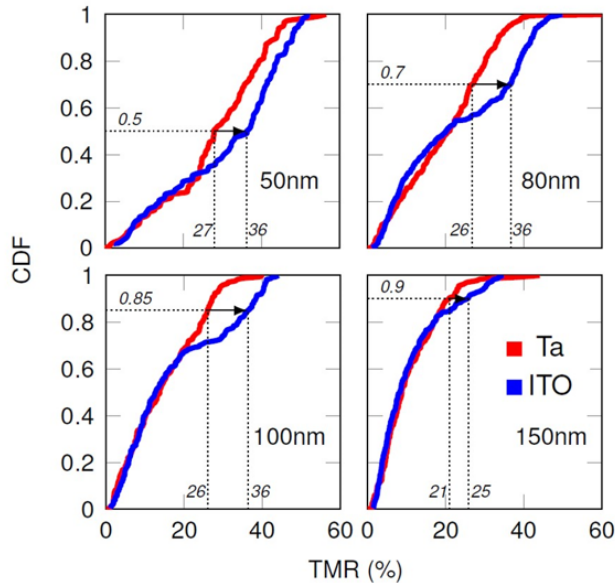


**Figure 8.** Cumulative distribution function (CDF) versus TMR for different MTJ diameters for the two processes (Ta & ITO).

material system of interest are magnetic tunnel junctions having a magnetic electrode that can be reversed by femto- or pico-second laser pulses. The development of such magnetic stacks integrated in a magnetic tunnel junction has been realized based on a [Tb/Co] multilayer stack that demonstrated all optical switching (AOS) properties [17]. In this section we will discuss the electrical results obtained on two different AOS tunnel junction stacks using the ITO process flow.

A first sample having a 15 repetition [Tb (0.87 nm)/ Co (1 nm)] multilayer electrode and a MgO barrier with  $R \times A$  below  $20 \Omega \cdot \mu m^2$  was fabricated. The full magnetic stack is shown in Figure 9 as well as the TMR versus measured  $R \times A$  for pillar nominal diameters from 80 nm to 150 nm. In this sample, an etch step was introduced to reduce possible contact resistance between the ITO hardmask and the ITO top lead. Compared to previous results in Figure 8, a

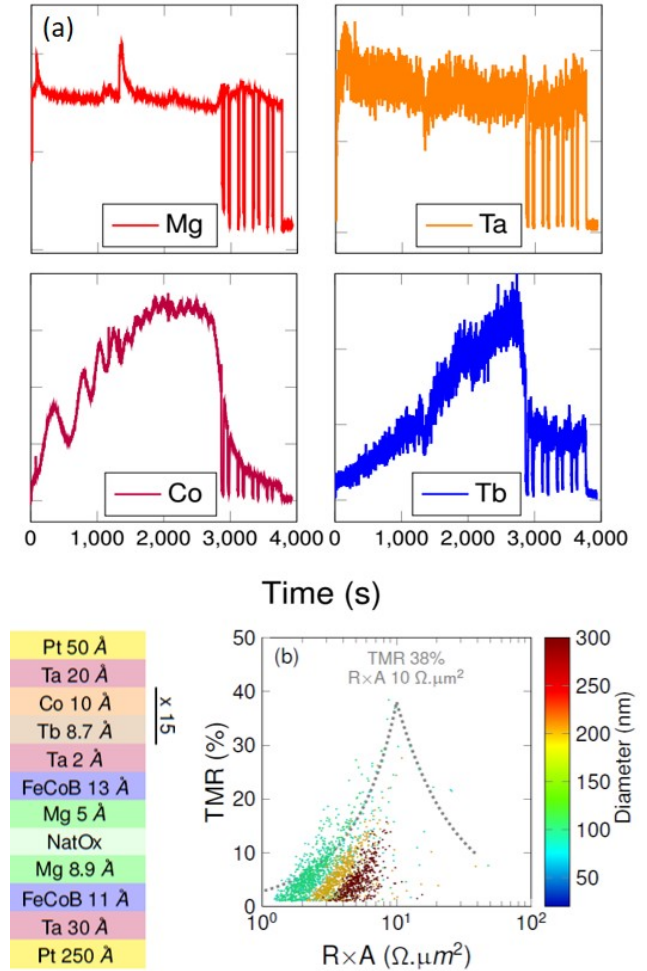


**Figure 9.** (a) SIMS monitoring during IBE etching of optically switchable CoFeB/MgO/CoFeB/Ta/[Tb/Co]<sub>15</sub> based MTJ pillar. (b) TMR plot with  $R \times A$  for different MTJ diameters.



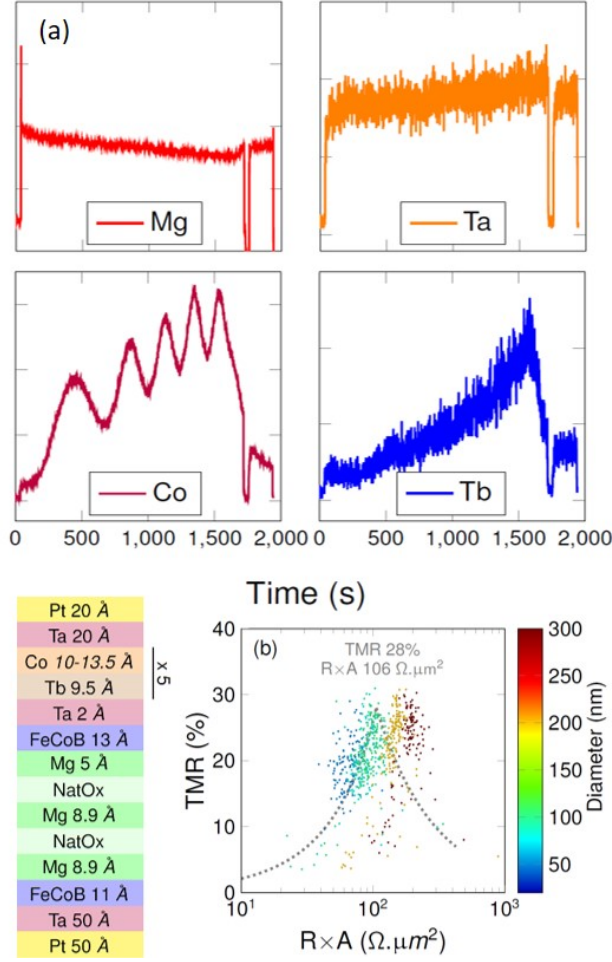


**Figure 10.** (a) SIMS monitoring during IBE etching of optically switchable CoFeB/MgO/CoFeB/Ta/[Tb/Co]<sub>5</sub> based MTJ pillar. (b) TMR plot with  $R \times A$  for different MTJ diameters.

clear improvement in the number of devices affected by the contact resistance is visible, with very few devices having  $R \times A$  values higher than the expected  $10\text{--}20 \Omega \cdot \mu m^2$ . A significant fraction of devices still suffers from reduced TMR limited by re-deposition shunting of the tunnel barrier. The IBE etch procedure, included a first initial etch step with an incidence angle  $20^\circ$  from the pillar vertical axis, until the MgO barrier followed by an alternating sequence of  $55^\circ$  and  $70^\circ$  angles (Figure 9(a)). Despite the grazing  $70^\circ$  etch angle, the total grazing angle etch time was not enough to prevent sidewall re-deposition after exposing the MgO barrier. Nonetheless, device yield was good with 54% of fabricated devices showing high squareness magnetoresistance loops.

A second sample having a 5 repetition [Tb 0.87 nm/ Co 1 nm] multilayer electrode and an MgO barrier with higher  $R \times A$  value of about  $150 \Omega \cdot \mu m^2$  achieved through an increase of the MgO thickness by

a double oxidation of two metallic Mg layers. The full magnetic stack is shown in Figure 10 as well as the device TMR versus measured  $R \times A$  values for pillar nominal diameters from 80 nm to 150 nm. For this sample the IBE etch procedure was modified. The initial etch step angle was increased to  $55^\circ$  until the observation Mg SIMS signal from the MgO barrier was observed, followed by a single 3 min  $70^\circ$  grazing angle etch (Figure 10(a)). The dispersion of TMR shows a significant reduction low TMR devices affected by re-deposition. There is still some dispersion around the wafer central value, but there is a clear TMR yield improvement with the implemented process changes in IBE etch and hardmask etch cleaning step ( $\approx 90\%$ ).

#### 4. Conclusion

Indium tin oxide (ITO) has been chosen as transparent conductive electrode to provide an optical access to the top electrode of magnetic tunnel junction devices. The morphology, electric and optical properties of the ITO films were evaluated for typical hardmask film thicknesses 50-300 nm, as well as the RIE patterning of the hardmask down to 50 nm critical dimensions. The ITO process flow was evaluated against a reference flow using a Ta hardmask. The ITO process showed a TMR yield at least as good as the reference flow with improvements of up to 10% for 80 and 100 nm diameter devices as observed in cumulative distribution data. Finally, magnetic tunnel junctions with all optical switching top electrode were fabricated with the developed ITO process flow. Device yields were improved by implementing optimized magnetic tunnel junction IBE etch and hardmask pre-clean steps. This process development is a necessary first step to demonstrate functionality and possible integration of all-optical-switching magnetic tunnel junctions.

#### Acknowledgments

We thank Dr. T. Chevolleau, T. Charvolin, C. Gomez and G. Gay for their help on the deposition and patterning of ITO. This research has received funding from the European Union's Horizon 2020 research and innovation program under FET-Open Grant Agreement No. 713481 (SPICE).

#### References

- [1] Bernard Dieny, Ronald B. Goldfarb, and Kyung-Jin Lee. *Introduction to Magnetic Random-Access Memory*. John Wiley & Sons, December 2016.
- [2] M. S. El Hadri, P. Pirro, C.-H. Lambert, S. Petit-Watelot, Y. Quessab, M. Hehn, F. Montaigne, G. Malinowski, and S. Mangin. Two types of all-optical magnetization switching mechanisms using

- femtosecond laser pulses. *Physical Review B*, 94(6):064412, August 2016.
- [3] Jun-Yang Chen, Li He, Jian-Ping Wang, and Mo Li. All-Optical Switching of Magnetic Tunnel Junctions with Single Subpicosecond Laser Pulses. *Physical Review Applied*, 7(2), February 2017.
- [4] Tadatsugu Minami. Transparent conducting oxide semiconductors for transparent electrodes. *Semiconductor Science and Technology*, 20(4):S35–S44, April 2005.
- [5] Z. Ghorannevis, E. Akbarnejad, and M. Ghorannevis. Structural and morphological properties of ITO thin films grown by magnetron sputtering. *Journal of Theoretical and Applied Physics*, 9(4):285–290, December 2015.
- [6] Mikio Mohri, Hiroaki Kakinuma, Masaaki Sakamoto, and Hideo Sawai. Plasma Etching of ITO Thin Films Using a CH<sub>4</sub>/H<sub>2</sub> Gas Mixture. *Japanese Journal of Applied Physics*, 29(Part 2, No. 10):L1932–L1935, October 1990.
- [7] D.Y. Kim, J.H. Ko, M.S. Park, and N.-E. Lee. Infinitely high etch selectivity during CH<sub>4</sub>/H<sub>2</sub>/Ar inductively coupled plasma (ICP) etching of indium tin oxide (ITO) with photoresist mask. *Thin Solid Films*, 516(11):3512–3516, April 2008.
- [8] Yue Kuo. Characterization of Indium Tin Oxide and Reactive Ion Etched Indium Tin Oxide Surfaces. *Japanese Journal of Applied Physics*, 29(Part 1, No. 10):2243–2246, October 1990.
- [9] Hideaki Agura, Akio Suzuki, Tatsuhiko Matsushita, Takanori Aoki, and Masahiro Okuda. Low resistivity transparent conducting Al-doped ZnO films prepared by pulsed laser deposition. *Thin Solid Films*, 445(2):263–267, December 2003.
- [10] N. Perrissin, S. Lequeux, N. Strelkov, A. Chavent, L. Vila, L. D. Buda-Prejbeanu, S. Auffret, R. C. Sousa, I. L. Prejbeanu, and B. Dieny. A highly thermally stable sub-20 nm magnetic random-access memory based on perpendicular shape anisotropy. *Nanoscale*, 10(25):12187–12195, 2018.
- [11] H. Kim, C. M. Gilmore, A. Piqué, J. S. Horwitz, H. Mattoussi, H. Murata, Z. H. Kafafi, and D. B. Chrisey. Electrical, optical, and structural properties of indium–tin–oxide thin films for organic light-emitting devices. *Journal of Applied Physics*, 86(11):6451–6461, December 1999.
- [12] Hideki Tanaka, Kazuhiko Ihara, Toshihiro Miyata, Hirotoshi Sato, and Tadatsugu Minami. Low resistivity polycrystalline ZnO:Al thin films prepared by pulsed laser deposition. *Journal of Vacuum Science & Technology A*, 22(4):1757–1762, July 2004.
- [13] T. Karasawa and Y. Miyata. Electrical and optical properties of indium tin oxide thin films deposited on unheated substrates by d.c. reactive sputtering. *Thin Solid Films*, 223(1):135–139, January 1993.
- [14] Bo Zhang, Xianping Dong, Xiaofeng Xu, and Jiansheng Wu. Preparation and characterization of tantalum-doped indium tin oxide films deposited by magnetron sputtering. *Scripta Materialia*, 58(3):203–206, February 2008.
- [15] Akio Suzuki, Tatsuhiko Matsushita, Takanori Aoki, Yoshitaka Yoneyama, and Masahiro Okuda. Pulsed Laser Deposition of Transparent Conducting Indium Tin Oxide Films in Magnetic Field Perpendicular to Plume. *Japanese Journal of Applied Physics*, 40(4B):L401, April 2001.
- [16] Keiji Nakamura, Tomonori Imura, Hideo Sugai, Michiko Ohkubo, and Katsutaro Ichihara. High-Speed Etching of Indium-Tin-Oxide Thin Films Using an Inductively Coupled Plasma. *Japanese Journal of Applied Physics*, 33(Part 1, No. 7B):4438–4441, July 1994.
- [17] L. Avilés-Félix, L. Álvaro Gómez, G. Li, C. S. Davies, A. Olivier, M. Rubio-Roy, S. Auffret, A. Kirilyuk, A. V. Kimel, Th. Rasing, L. D. Buda-Prejbeanu, R. C. Sousa, B. Dieny, and I. L. Prejbeanu. Integration of Tb/Co multilayers within optically switchable perpendicular magnetic tunnel junctions. *AIP Advances*, 9(12):125328, December 2019.